remote sensing

MDPI

Article

Fusion of Landsat-8/OLI and GOCI Data for Hourly Mapping of Suspended Particulate Matter at High Spatial Resolution: A Case Study in the Yangtze (Changjiang) Estuary

Yanqun Pan, Fang Shen * and Xiaodao Wei

State Key Laboratory of Estuarine and Coastal Research, East China Normal University, Shanghai 200062, China; panyq213@163.com (Y.P.); weixiaodao106@163.com (X.W.)

* Correspondence: fshen@sklec.ecnu.edu.cn; Tel.: +86-021-6223-3467

Received: 21 November 2017; Accepted: 18 January 2018; Published: 23 January 2018

Abstract: Suspended particulate matter (SPM) concentrations ([SPM]) in the Yangtze estuary, which has third-order bifurcations and four outlets, exhibit large spatial and temporal variations. Studying the characteristics of these variations in [SPM] is important for understanding sediment transport and pollutant diffusion in the estuary as well as for the construction of port and estuarine engineering structures. The 1-h revisit frequency of the Geostationary Ocean Color Imager (GOCI) sensor and the 30-m spatial resolution of the Landsat 8 Operational Land Imager (L8/OLI) provide a new opportunity to study the large spatial and temporal variations in the [SPM] in the Yangtze estuary. In this study, [SPM] images with a temporal resolution of 1 h and a spatial resolution of 30 m are generated through the product-level fusion of [SPM] data derived from L8/OLI and GOCI images using the Spatial and Temporal Adaptive Reflectance Fusion Model (STARFM). The results show that the details and accuracy of the spatial and temporal variations are maintained well in the [SPM] images that are predicted based on the fused images. Compared to the [SPM] observations at fixed field stations, the mean relative error (MRE) of the predicted SPM is 17.7%, which is lower than that of the GOCI-derived [SPM] (27.5%). In addition, thanks to the derived high-resolution [SPM] with high spatiotemporal dynamic changes, both natural phenomena (dynamic variation of the maximum turbid zone) and human engineering changes leading to the dynamic variability of SPM in the channel are observed.

Keywords: data fusion; GOCI; landsat-8; Yangtze estuary; remote sensing; suspended particulate matter

1. Introduction

Estuaries are the interfaces of land–sea interactions, areas of intensive human activity, and the "sources" and "sinks" of material fluxes in oceans and river basins [1]. [SPM] in estuaries are important parameters for analyzing the variations in substrate erosion and deposition and estimating material fluxes from the rivers to the seas and marine environments [2,3]. With an annual mean runoff volume of 9.051×10^9 m^3, the Yangtze River is the largest river in China and the third largest in the world [4]. The Yangtze estuary is a multi-order bifurcation, island-type dynamic estuary with a moderate tidal range and a complex estuarine delta landform [5]. Due to the differences in the flow diversion ratio, tidal current, and channel boundary, there are substantial spatial and temporal variations in the distribution of [SPM] between the channels [6,7]. Several studies have shown that recent variations in the amounts of water and sediment flowing into the Yangtze River Basin have exerted a relatively significant impact on the water–sediment environment, the sea-bound waterways, and the evolution

of the riverbed and shoals in the estuary [7–9]. Therefore, studying the characteristics of the spatial and temporal variations in [SPM] in the channels and waterways in the Yangtze estuary can provide monitoring support for research on the hydrological, geomorphological, and dynamic environments, as well as for the construction of estuarine engineering structures and ports.

[SPM] values derived from satellite data contain richer spatial information than those derived from conventional measurement methods (e.g., on-board ship measurements and station observations). The Yangtze estuary contains numerous channels and branches, which results in complex dynamic conditions and large spatial and temporal variations in the [SPM]. Dynamic remote sensing observations of [SPM] at the river channel and waterway level requires the support of sensors with high spatial and temporal resolutions. However, a single satellite sensor is currently unable to meet this requirement. The Operational Land Imager carried by the Landsat 8 satellite is capable of monitoring the variations in the spatial distribution of the [SPM] in an estuary with a 30-m spatial resolution, a high signal-to-noise ratio, and shortwave infrared (SWIR) channels [10–13]. However, the 16-day revisit period prevents L8/OLI data from meeting the requirements for studying highly dynamic variations in the [SPM]. With the ability to provide eight scenes per day with a 1-h temporal resolution, the Geostationary Ocean Color Imager (GOCI) meets the requirements for studying the daily variations in the [SPM] [14,15]. However, due to its 500-m spatial resolution, the GOCI is unable to show the details of small-scale distributions of the [SPM] in the channels and waterways in the Yangtze estuary, such as the impacts of dredging projects on the spatial variations in the [SPM] [16]. The GOCI and L8/OLI both have unique advantages and disadvantages in detecting dynamic spatial and temporal variations in the [SPM] due to their high spatial and temporal resolutions, respectively. This study focuses on how to generate SPM images with both the high temporal resolution provided by the GOCI and the high spatial resolution provided by the L8/OLI using an image fusion method (i.e., how to integrate the advantages of the GOCI and the L8/OLI).

Since the 1990s, numerous researchers have proposed various spatial and temporal image fusion models, including the classical Spatial and Temporal Adaptive Reflectance Fusion Model (STARFM) [17], the enhanced STARFM (ESTARFM) [18], the Spatial Temporal Adaptive Algorithm for Mapping Reflectance Change (STAARCH) [19], and the Sparse Representation-based Spatiotemporal Reflectance Fusion Model (SPSTFM) [20]. Zhang et al. [21] noted that the STARFM and the ESTARFM are more suitable for temporal variation- and spatial variation-dominated areas, respectively, whereas the SPSTFM is more suitable for studying land-cover and phenological changes. Spatial and temporal image fusion techniques are mostly used in remote sensing of land surfaces (e.g., detection of vegetation changes) but are seldom used in ocean color remote sensing. Vanhellemont et al. [22] predicted the Moderate Resolution Imaging Spectroradiometer (MODIS) reflectance by establishing the simple linear temporal variability of the Spinning Enhanced Visible and IR Imager (SEVIRI) reflectance and used the fused reflectance images to study the daily variations in the turbidity of the waters of the North Sea in Europe.

In this study, [SPM] images with high spatial and temporal resolutions are generated from GOCI- and L8/OLI-derived [SPM] images based on the STARFM algorithm. The main content of this study includes (1) establishing a method and procedure for the fusion of [SPM] based on GOCI and L8/OLI images (Section 3); (2) analyzing the remote sensing reflectance R_{rs} and [SPM] derived from GOCI and L8/OLI images (Section 4); and (3) validating the [SPM] derived from the fused images with real-time data acquired at field automatic observation stations (OBSs) and analyzing the error sources and limitations [SPM] (Section 5).

2. Study Area and Data Sets

2.1. SPM Characteristics of the Study Area

The Yangtze estuary is divided by Chongming Island into the South Branch and North Branch. The South Branch is further divided by Changxing Island and Hengsha Island into the South Channel

and North Channel. The South Channel is then divided by the Jiuduansha Shoals into the South Harbor and the North Harbor. As a result, the Yangtze estuary has third-order bifurcations with four outlets (Figure 1). The spatial distribution of the [SPM] varies substantially between the channels within the estuary. The surface [SPM] generally increase from the South Branch to the largest turbid zone in the estuary. High [SPM] occur in the South and North Channels and in the largest turbid zone in the North Branch. The [SPM] in the south branch are the lowest, followed by those in the South and North Harbors [5]. Based on hydrological measurements, the multi-year mean [SPM] in the north branch is 0.53 g L^{-1} during the flood season and 1.09 g L^{-1} during the dry season. In comparison, the multi-year mean [SPM] in the south branch is approximately 0.23 g L^{-1} during the flood season and only approximately 0.1 g L^{-1} during the dry season [5]. The multi-year mean [SPM] in the North Branch is approximately twice that in the South Branch during the flood season and more than 10 times that in the South Branch during the dry season [5,6]. In recent years, there has been a sharp decrease in the amount of sediment flowing into the Yangtze River Basin and a decrease in the [SPM] in the channels of the South Branch [5,6]. However, as the intensity of dynamic land–sea interactions changes, the [SPM] in the mouth bar area have been increasing gradually. The in the other channels exhibit different variations due to the combined effects of sediment flowing into the river basin and resuspension [5,6,23,24]. As a result of the seasonal variations in the amounts of water and sediment flowing into the Yangtze River Basin, the in the estuary of the Yangtze River exhibit notable periodic variations between the flood and dry seasons. In addition, the tidal current has a relatively important impact on the Yangtze estuary. Because the spring tide velocities are much greater than the neap tide velocities, the mean is higher during the spring tides than during the neap tides. As a result of considerable variations in the flood and ebb tides in the Yangtze estuary, the [SPM] in the waters also exhibit notable tidal periodic variations [5,24].

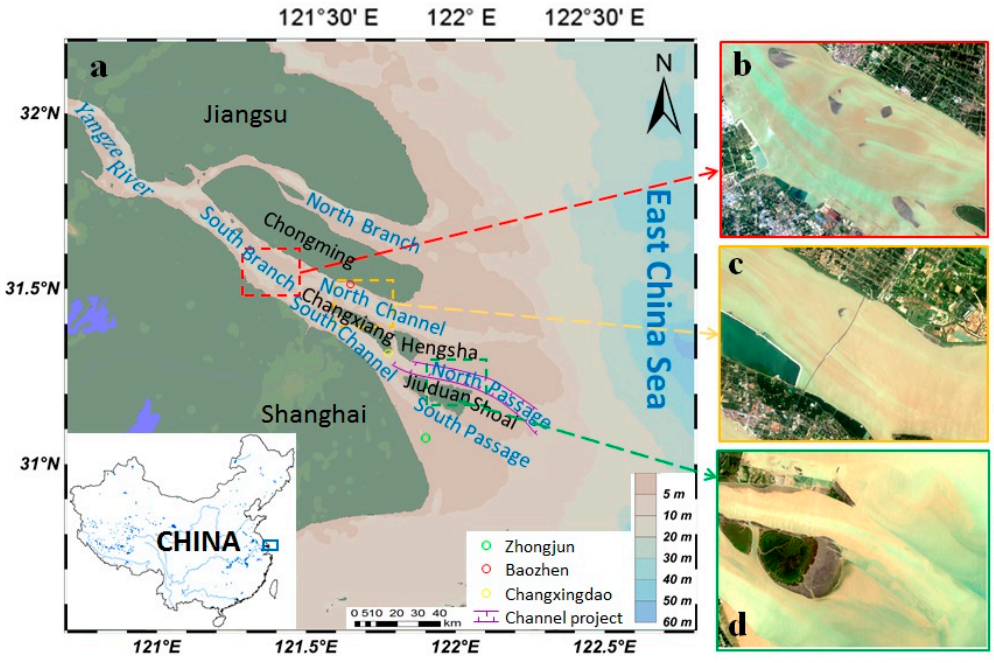

Figure 1. Location and detailed images of the study area. (**a**) Location of the study area. The purple line represents the channel and silt embankment, and the red and yellow circles represent the locations of Baozhen and Changxingdao fixed field stations, respectively. The red circle represents the Zhongjun tide gauge station. The legend of the water depth is also included; (**b**–**d**) Detailed images of the estuary in the vicinity of the South Branch, Chongming Bridge and South and North Harbor, respectively.

2.2. Satellite Images

In 2010, South Korea launched the world's first geostationary orbit ocean color sensor, GOCI [25]. The observation range of GOCI is 2500 km × 2500 km, which covers the Yangtze estuary, China's Bohai Sea, the Yellow Sea, the East China Sea, and other waters. The GOCI's spectral range covers the visible to near-infrared (NIR) range with eight wavebands centered at 412 nm, 443 nm, 490 nm, 555 nm, 660 nm, 680 nm, 745 nm, and 865 nm. The relative spectral response (RSR) curves for the eight wavebands are shown as solid lines in Figure 2. The GOCI has a spatial resolution of 500 m and is located in a geosynchronous orbit approximately 35,786 km above the equator. The GOCI collects one image every other hour between 08:00 and 15:00 h (Beijing time; all times in this study are in Beijing time) daily.

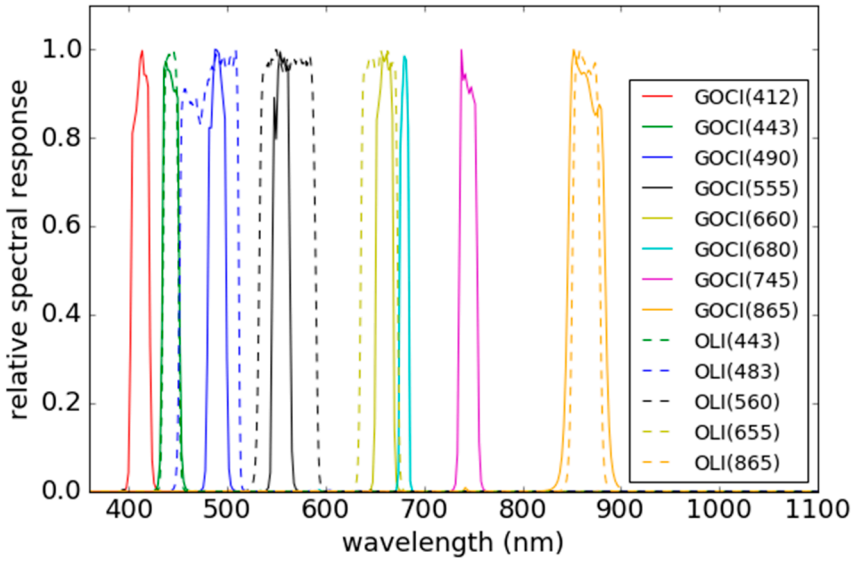

Figure 2. Relative spectral responses of GOCI and L8/OLI. The central wavelengths are shown in the legend.

Launched in February 2013, Landsat-8 is a sun-synchronous orbiting satellite with an orbital height of 705 km and an orbital inclination of 98.2° that orbits the Earth every 98.9 min with a transit time of 10:30 and a revisit period of 16 days. Landsat-8 carries two sensors: the Operational Land Imager (OLI) and the Thermal Infrared Radiometer Suite (TIRS). L8/OLI has eight multispectral channels with a spatial resolution of 30 m, and the central wavelengths are 443 nm, 483 nm, 561 nm, 655 nm, 865 nm, 1609 nm, and 2201 nm. The RSR curves in the visible and NIR bands are shown as dashed lines in Figure 2. Although L8/OLI is not designed for ocean monitoring, its advantages of high spatial resolution and the increased number of bands, combined with its improved signal-to-noise ratio and data quality, make it increasingly used in ocean color remote sensing research and especially in estuarine and coastal research [26–33].

Ocean color products with different levels (Levels 1–3) derived from GOCI and L8/OLI are available at the Korean Ocean Satellite Center's (KOSC) official website (http://kosc.kiost.ac/eng/p10/kosc_p11.html) and the EarthExplorer website (http://earthexplorer.usgs.gov/), respectively. Detailed information about the classification of satellite ocean color products can be found on the NASA website (https://oceancolor.sci.gsfc.nasa.gov/products/). Four high quality images of L8/OLI and GOCI L1B products, including radiance data at the top of atmosphere (TOA) from August to November 2013 (13 August, 29 August, 14 September and 17 November), were used in this study (Table 1).

Table 1. Dates, times, and numbers of the L8/OLI and GOCI L1B images used in this study.

Date	Platform/Sensor	Number of Scenes	Time (Beijing Time)
13 August 2013	L8/OLI	1	10:30
	GOCI	6	10:30 11:30 12:30 13:30 14:30 15:30
29 August 2013	L8/OLI	1	10:30
	GOCI	5	08:30 09:30 10:30 11:30 12:30
14 September 2013	L8/OLI	1	10:30
	GOCI	4	08:30 09:30 10:30 11:30
17 November 2013	L8/OLI	1	10:30
	GOCI	8	08:30 09:30 10:30 11:30 12:30 13:30 14:30 15:30

2.3. SPM Dataset Observed by Obss at Fixed Field Stations

To validate the [SPM] derived from the images, we collected SPM datasets from fixed field stations where the water turbidity is automatically recorded using D&A Tech optical backscatter instruments (OBSs). Commonly, the OBSs directly measure turbidity in the Nephelometric Turbidity Unit (NTU). To obtain the [SPM], we needed to calibrate their relationship. This study used the averages of the derived from the relationships reported by Xue et al. [34] and Zhao et al. [24] as the measured. After screening the data quality of the fixed stations, this study used the data from Changxingdao and Baozhen, which are of better quality. The locations of Changxingdao (121°45′19.44″E, 31°19′33.84″N) and Baozhen (121°36′12.70″E, 31°31′21.41″N) are shown as red and yellow circles, respectively, in Figure 1.

The OBS collects NTU data every other 15 s. To match the image, we selected the average of the measurements during the scan time of each image as the station measurement. For example, the first GOCI image was acquired from approximately 00:16 (UTC) to 00:45 h (UTC). Therefore, we selected the average of the measured station data between 00:16 (UTC) and 00:45 h (UTC) as the image-matching measurement. In addition, the median of the L8/OLI-estimated SPM was calculated in a 3 × 3 pixel window as the image-matching measurement. A detailed description of the relationship between NTU and [SPM] and the method of building match-ups can be found in Pan et al. [35].

3. Methodology

3.1. Atmospheric Correction of L8/OLI and GOCI Images

The key point of the atmospheric correction of satellite imagery is to estimate the reflectance of aerosols, which is mainly determined by the aerosol type and the aerosol optical depth (AOD). Due to the invalid assumption of dark pixels in extremely turbid waters and the impact of absorbing aerosols, estimating the aerosol type and AOD using well-known algorithms, such as iterative-based algorithms, is difficult. For the extremely turbid waters in the Yangtze estuary, Pan et al. [35] proposed the Enhanced Spectral Optimization Algorithm (ESOA) based on a coupled aerosol-water model. The coupled model combines an Aerosol Robotic Network (AERONET)-based aerosol model and a simple semi-empirical radiative transfer (SERT) model [36]. The coupled model includes four unknown parameters: the relative humidity (RH), fine-mode fraction (FMF), AOD in the NIR wavelength $\tau_a(865)$ and [SPM]. The RH and FMF represent the aerosol type, whereas the SPM determines the remote sensing reflectance spectrum. The four unknown parameters are estimated by a global optimization approach based on a genetic algorithm (GA) without any initial inputs. Because GAs are very time consuming, a spatially homogenous aerosol type is assumed for the operational processing of satellite imagery, and the satellite imagery is corrected in two steps:

1. The aerosol type and $\tau_a(865)$ are estimated from a cloud-free and turbid pixel based on the global optimization algorithm, GA.
2. By assuming a spatially homogenous aerosol type, the unknowns in the coupled model are reduced to two ($\tau_a(865)$ and SPM). These two unknowns are then optimized pixel by pixel using

the fast optimization algorithm Levenberg-Marquardt (LM) with the initial inputs estimated by Step 1.

This algorithm is imbedded in the Level-2 generator (l2gen) program in the Sea-viewing Wide Field-of-View Sensor Data Analysis System (SeaDAS) software; therefore, the calculations of the Rayleigh scattering, aerosol scattering, white cap, glint, bi-directional reflectance distribution function (BRDF) correction factor and other terms included in the atmospheric correction procedure are completely based on l2gen. For detailed calculations of these terms, see Mobley's description [37]. The validation with match-ups in the Yangtze estuary and the comparison with the GOCI data processing system (GDPS) suggested that ESOA is an alternative operational tool for the atmospheric correction of satellite images over highly turbid waters [35]. In this study, the aerosol type and $\tau_a(865)$ of the GOCI imagery are estimated using the ESOA algorithm.

For L8/OLI data, Vanhellemont et al. [33,38] reported an effective method for the atmospheric correction of high-turbidity nearshore waters using two SWIR bands (1609 nm and 2201 nm). This method was implemented in a software suite called ACOLITE, which is available on the Royal Belgian Institute of Natural Sciences (RBINS) website (https://odnature.naturalsciences.be/remsem/software-and-data/acolite). We processed L8/OLI images using ACOLITE (v 20160120.0) and found that there were a large number of negative values of R_{rs}, which indicates that the SWIR-based atmospheric correction algorithm may produce large errors over the optically complex water bodies with high turbidity in the Yangtze estuary.

The L8/OLI images used in this study were acquired at 10:30 h, which is nearly the same time as the third daily scene of GOCI images (acquired at 10:30); thus, it is reasonable to assume that the two images share the same spatial distributions of aerosol type and AOD. Based on this assumption, it is not necessary to estimate the aerosol parameters for L8/OLI again, so we corrected the L8/OLI L1B images using the RH, FMF, and $\tau_a(865)$ derived from the GOCI images (10:30) to the l2gen program directly. The original l2gen program cannot correct images with fixed RH, FMF, and aerosol optical thickness (AOT) values as input parameters; therefore, we extend the l2gen by programming. The OLI images are then processed using the extended l2gen program.

3.2. SPM Retrieval of GOCI and L8/OLI

In this study, a semi-empirical model called SERT was used to retrieve [SPM] from GOCI and L8/OLI data. The SERT model builds the relationship between the remote sensing reflectance R_{rs} and [SPM] based on a two-stream approximation radiative transfer model [36]. The forward form of SERT is as follows:

$$R_{rs} = f([SPM]) = \frac{\alpha\beta[SPM]}{1 + \beta[SPM] + \sqrt{1 + 2\beta[SPM]}}, \quad (1)$$

where α and β are wavelength-dependent coefficients, which can be recalibrated and optimized by in situ simultaneous measurements of R_{rs} and the [SPM]. The inversion form is as follows:

$$[SPM] = f_{inverse}(R_{rs}) = \frac{(2\alpha/\beta)R_{rs}}{(\alpha - R_{rs})^2}, \quad (2)$$

In this study, α and β were calibrated using in situ measurements from the Yangtze estuarine and coastal waters from 2013 to 2015. Radiometric measurements were recorded by the Hyperspectral Surface Acquisition System (HyperSAS, Satlantic Inc., Halifax, Nova Scotia, Canada) and consist of the sea-surface radiance (L_t), sky radiance (L_i) and solar irradiance (E_s) from 350 to 900 nm in 136 spectral channels. Details about the sensors' mounting and observation geometries can be found in Shen et al. [36,39]. R_{rs} was calculated by [40,41]:

$$R_{rs} = \frac{L_t - \rho L_i}{E_s}, \quad (3)$$

where ρ is the sea surface reflectance factor, which is correlated to the solar zenith angle and surface roughness. Additional details about the R_{rs} calculation can be found in Sokoletsky and Shen [42]. The [SPM] were determined gravimetrically by filtering the surface water samples on 0.7-µm Whatman GF/F glass fiber filters. The blank and sample-filled filters were rinsed with Milli-Q water to remove salts, dried and then reweighed on a high-precision balance in the laboratory. After performing quality control, 66 R_{rs}–SPM data pairs collected on cruises between 2013 and 2015 were available (for a detailed description of the R_{rs}–SPM data pairs, see Shang et al. [43]). The parameters α and β were fitted from the R_{rs}–SPM data pairs using least squares regression. Table 2 lists the values of α and β at the central wavelengths of the GOCI and L8/OLI bands. Because the longest wavelength of R_{rs} is measured at 858 nm, the values of α and β in Table 2 at 865 nm are approximated at 858 nm. Figure 3 shows the $R_{rs}(\lambda)$ spectrum at the central wavelength of GOCI bands calculated by the SERT model.

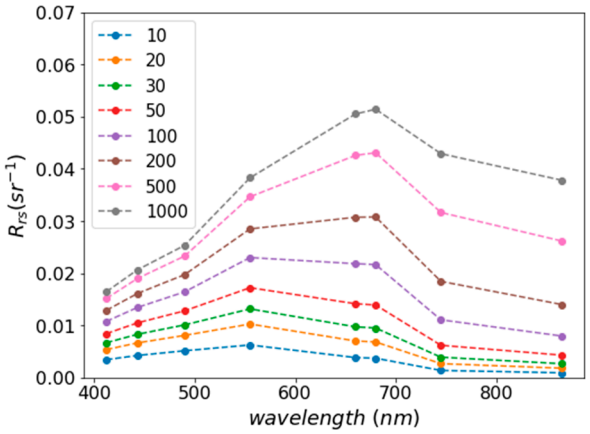

Figure 3. Remote sensing reflectance spectrum $R_{rs}(\lambda)$ calculated by the semi-empirical radiative transfer (SERT) model (shown in the legend in g m^{-3}).

Table 2. Two parameters of the SERT model at the GOCI and L8/OLI bands.

Sensor	Central Wavelength (nm)	α	β
GOCI	412	0.0201	49.6982
GOCI, L8/OLI	443	0.0253	48.3820
L8/OLI	483	0.0302	47.4212
GOCI	490	0.0311	47.5101
GOCI	555	0.0488	33.7132
L8/OLI	561	0.0509	32.2256
L8/OLI	655	0.0762	11.5345
GOCI	660	0.0771	11.0158
GOCI	680	0.0797	10.2475
GOCI	745	0.0954	2.9698
GOCI, L8/OLI	865	0.1038	1.8042

Considering the sensitivity of [SPM] to R_{rs} at different wavelengths, Shen et al. [36,39,44] proposed an inversion scheme based on band shifting for SPM retrieval from satellite imagery in the Yangtze estuary. In this study, we used the three-band shifting scheme for SPM retrieval from GOCI and L8/OLI data. The three selected bands were 555 nm, 660 nm, and 865 nm for GOCI and 561 nm, 655 nm, and 865 nm for L8/OLI. The inversion formulas are as follows:

$$[\mathrm{SPM}]^{\mathrm{GOCI}} = \begin{cases} f_{inverse}(\mathrm{R_{rs}}(555)) \; if \; \mathrm{R_{rs}}(660) < 0.012 \\ f_{inverse}(\mathrm{R_{rs}}(660)) \; else \; if \; \mathrm{R_{rs}}(865) < 0.02 \\ f_{inverse}(\mathrm{R_{rs}}(865)) \qquad else \end{cases}, \tag{4}$$

$$[\mathrm{SPM}]^{\mathrm{OLI}} = \begin{cases} f_{inverse}(\mathrm{R_{rs}}(561))\ if\ \mathrm{R_{rs}}(655) < 0.012 \\ f_{inverse}(\mathrm{R_{rs}}(655))\ else\ if\ \mathrm{R_{rs}}(865) < 0.02 \\ f_{inverse}(\mathrm{R_{rs}}(865)) \qquad else \end{cases}, \quad (5)$$

where $[\mathrm{SPM}]^{\mathrm{GOCI}}$ and $[\mathrm{SPM}]^{\mathrm{OLI}}$ refer to [SPM] derived from GOCI and L8/OLI data, respectively.

3.3. The Spatial and Temporal Fusion Model STARFM

The STARFM algorithm was proposed by Gao et al. [17]. The algorithm is based on the premise that both coarse- and fine-resolution imagery observe the same object and are biased by a constant error. This error depends on the characteristics of a pixel and is systematic over short temporal intervals. Therefore, if a base coarse-fine image pair is available at the same time, this error can be calculated for each pixel in the image. These errors can then be applied to the coarse-resolution imagery of a predicted time to obtain fine-resolution imagery like the prediction image of that time. By introducing additional information from neighboring pixels, the STARFM model predicts the value of the central pixel with the fine-resolution imagery at the prediction time using a moving window and weighting functions. The STARFM model has been used in several applications, such as in detecting land-cover change by blending MODIS and Landsat surface reflectances [17,45] and generating daily land surface temperatures at the Landsat resolution by fusing Landsat and MODIS data [46]; however, it has not been applied to water. In this study, we apply it to predict the hourly [SPM] at a spatial resolution of 30 m by blending L8/OLI- and GOCI-derived [SPM]. Generally, there are two main differences between land and water when blending satellite imagery: the dynamic variation of water, especially in estuarine areas, is greater than that of land cover, and land cover images may have mutations, such as from forest to plowed areas, whereas water areas are always continuous. The STARFM model has been shown to be capable of capturing changes in patterns by searching similar pixels in the moving window [17,45]. In this study, although [SPM] and its spatial distribution patterns in the Yangtze estuary change hourly, it is easy for STARFM to search similar pixels in a certain window size. Therefore, it is reasonable to apply the STARFM model to SPM prediction in the Yangtze estuary.

In this case, the coarse- and fine-resolution images are of [SPM] derived from GOCI and L8/OLI data, respectively. The fusion algorithm is expressed as follows:

$$[\mathrm{SPM}]^{\mathrm{OLI}}(x_{w/2}, y_{w/2}, T_2) = \sum_{i=1}^{w}\sum_{j=1}^{w} W_{ij}([\mathrm{SPM}]^{\mathrm{GOCI}}(x_i, x_j, T_2) + [\mathrm{SPM}]^{\mathrm{OLI}}(x_i, y_i, T_1) - [\mathrm{SPM}]^{\mathrm{GOCI}}(x_i, y_i, T_1)), \quad (6)$$

where w is the size of the moving window, $x_{w/2}$ and $y_{w/2}$ are the coordinates of the center pixels in the moving window, $[\mathrm{SPM}]^{\mathrm{OLI}}(x_{w/2}, y_{w/2}, T_2)$ refers to the predicted SPM pixel value derived from L8/OLI at T_2, $[\mathrm{SPM}]^{\mathrm{OLI}}(x_i, y_i, T_1)$ and $[\mathrm{SPM}]^{\mathrm{GOCI}}(x_i, y_i, T_1)$ are the SPM pixel values derived from the L8/OLI and GOCI data, respectively, at position (i, j) in the moving window at time T_1, $[\mathrm{SPM}]^{\mathrm{GOCI}}(x_i, x_j, T_2)$ represents the SPM pixel value derived from the GOCI data at time T_2, W_{ij} is the weight of the pixel at position (i, j) in the window, which determines the contribution of the pixel at (i, j) to the predicted central pixel, and W_{ij} is related to three distances: the spectral distance, spatial distance and temporal distance (for a detailed calculation of the weights, see Gao et al. [1]). The moving window size w influences the prediction. To capture the changes of small objects (SPM distribution patterns), one can increase the size w. In this study, w is set to 1500 m, which is 3 × 3 GOCI pixels (500-m resolution) or 50 × 50 L8/OLI pixels (30-m resolution). The STARFM source code can be freely downloaded from the US Department of Agriculture (USDA) Agricultural Research Service (ARS) official website (https://iapreview.ars.usda.gov/services/software/download.htm).

3.4. The Fusion Procedure

This study aims to predict daily [SPM] images for the study area with a 30-m spatial resolution (L8/OLI) at 08:30, 09:30, 11:30, 12:30, 13:30, 14:30 and 15:30 h based on the L8/OLI image (10:30 h)

and GOCI images of eight scenes for each day. Figure 4 shows the [SPM] image fusion procedure. The specific steps are as follows:

1. The GOCI L1B TOA radiance images are processed using the ESOA method to estimate the aerosol and atmospheric corrections. The aerosol parameters (RH, FMF, and $\tau_a(865)$) and R_{rs} in each GOCI image are thus obtained.
2. The L8/OLI L1B TOA radiance images are processed for atmospheric correction by extending the l2gen program with the aerosol parameters derived from the GOCI images (10:30 h) as the input parameters. Before correcting the L8/OLI images, the $\tau_a(865)$ images derived from the GOCI images (10:30 h) are resampled to the resolution of L8/OLI and registered.
3. The [SPM] are estimated based on R_{rs} using a SERT-based model for deriving [SPM]. In Figure 4, $[SPM]^{GOCI}$ and $[SPM]^{OLI}$ are the GOCI- and L8/OLI-derived [SPM], respectively.
4. The GOCI-derived $[SPM]^{GOCI}$ images are resampled to the L8/OLI's 30-m spatial resolution and registered. The image resampling and registration were performed using the collocation tool in the SeaDAS software. The nearest neighbor method was used as the resampling method.
5. The registered and resampled L8/OLI (10:30 h)- and GOCI-derived [SPM] images were used to establish base image pairs. The [SPM] images at 08:30, 09:30, 11:30, 12:30, 13:30, 14:30, and 15:30 h were predicted using the STARFM model. The predicted SPM images have the temporal resolution of the GOCI and the spatial resolution of the L8/OLI.

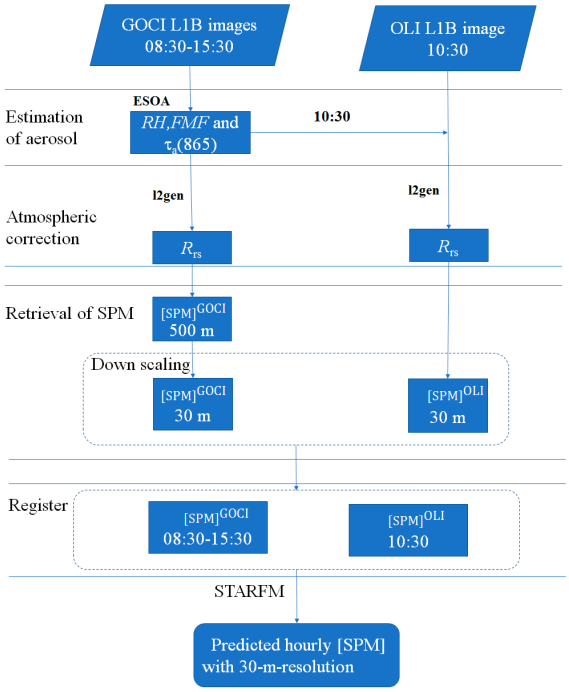

Figure 4. Flowchart of the fusion procedure. $[SPM]^{GOCI}$ and $[SPM]^{OLI}$ refer to the [SPM] derived from GOCI and L8/OLI, respectively.

3.5. Data Analysis

The mean relative error (MRE) is used to quantitatively evaluate the goodness-of-fit of the derived and measured [SPM]. The MRE is calculated as follows:

$$R_{rs} = \frac{1}{n}\sum_{i=1}^{n}\frac{\left|V^i_{retrieved} - V^i_{insitu}\right|}{V^i_{insitu}} \times 100\%, \quad (7)$$

where n refers to the number of samples, i refers to the ith sample, and $V_{retrieved}$ and V_{insitu} are the retrieved and true values, respectively.

4. Results

4.1. R_{rs} and [SPM] Derived from GOCI and L8/OLI

The GOCI and L8/OLI L1B images in this study were all processed using the method described in Sections 3.1 and 3.2, and images of R_{rs} and [SPM] were obtained. Here, the images at 10:30 hon August 29 are used as an example for the analysis. Figure 5a–e shows images of R_{rs} in the Yangtze estuary at the GOCI bands (490 nm (a), 555 nm (b), 660 nm (c), 745 nm (d) and 865 nm (e)). Figure 5f shows the derived $[SPM]^{GOCI}$ image. As shown in the $[SPM]^{GOCI}$ image, the [SPM] in the Yangtze Estuary ranged from 0.01 to 0.5 g L^{-1}, with the minimum values are generally observed in the outsides and the maximum values are generally observed near the North Harbor. Compared to the South and North Harbors and the South and North channels in the downstream area, the [SPM] in the South Branch are relatively low (approximately 0.02 g L^{-1}), which is consistent with the multi-year mean hydrological observation data. However, the [SPM] in the North Branch are relatively low compared to those in the South Branch.

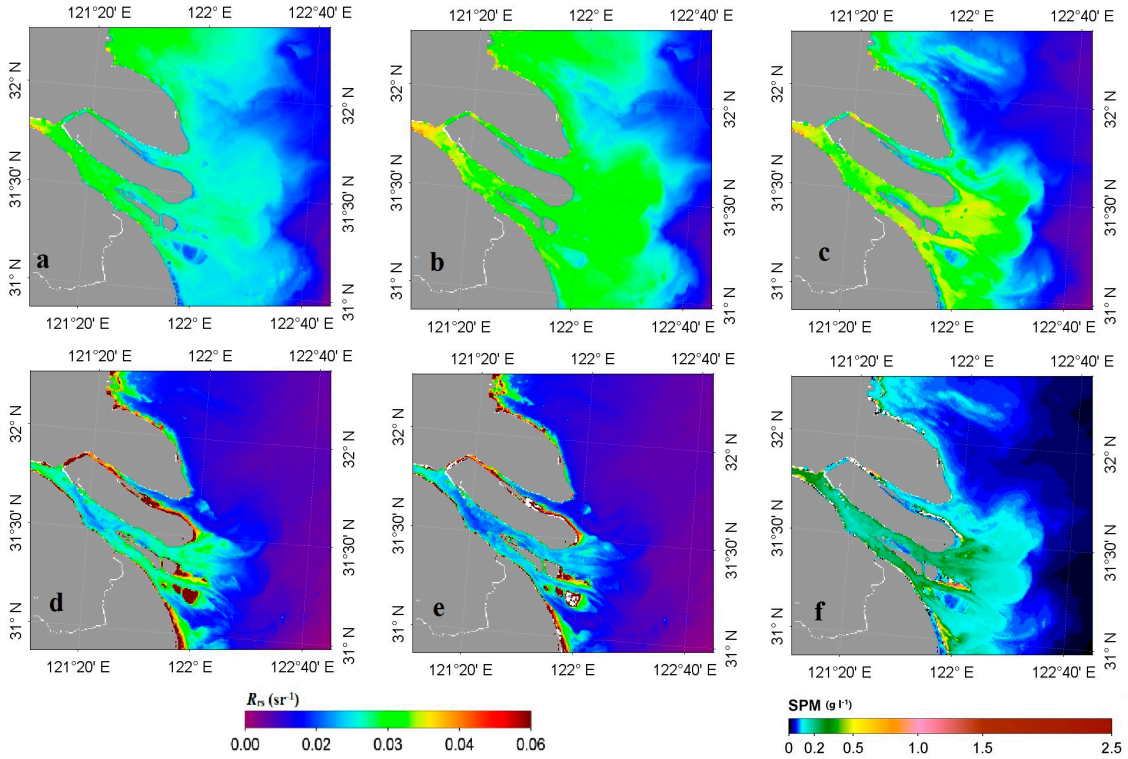

Figure 5. R_{rs} (λ) and SPM retrieved from the GOCI image at 10:30 h, 29 August, 2013 using Enhanced Spectral Optimization Algorithm (ESOA) and SERT: (**a**) 490 nm; (**b**) 555 nm; (**c**) 660 nm; (**d**) 745 nm; (**e**) 865 nm; (**f**) [SPM]. The land masks with 50-m resolution in SeaDAS were used.

A comparison of the R_{rs} images at the L8/OLI bands (481 nm, 560 nm, 655 nm and 865 nm) in the Yangtze estuary at 10:30 h on August 29 (Figure 6) with the GOCI-derived R_{rs} images (Figure 5) shows that the L8/OLI-derived R_{rs} values are generally higher. Figure 7 shows images of $[SPM]^{OLI}$ in the Yangtze estuary. The spatial distribution of $[SPM]^{OLI}$ is generally consistent with that of $[SPM]^{GOCI}$. However, the $[SPM]^{OLI}$ values are slightly higher than the $[SPM]^{GOCI}$ values. The $[SPM]^{OLI}$ values are as high as 0.6 g L^{-1} in the largest turbid zone. Figure 7b–d show the details of the distribution of the [SPM] in the red boxes numbered 1–3 in Figure 7a. Clearly, the $[SPM]^{OLI}$ image with a 30-m

spatial resolution shows more details about the spatial distribution of the [SPM] within and outside the estuary of the Yangtze River. Figure 7b shows the spatial distribution of the [SPM] near the Chongming Bridge (the shoals in the river are marked with red circles). There is a notable spatial variation in the [SPM] in this area; the [SPM] are much lower upstream of the bridge than downstream. Figure 8a shows a comparison of the retrieved [SPM] on section lines L1 and L2 shown in Figure 7b, which are located upstream and downstream of the Chongming Bridge, respectively. As shown in Figure 8a, the [SPM] on line L1 are much higher than those on the line L2. This may be attributed to the change in the hydrodynamic environment caused by the bridge piers. In addition, the shoals alter the spatial distribution of the [SPM]. The [SPM] are much lower downstream of the shoals than upstream. Figure 7c shows the spatial distribution of the [SPM] in the South Branch (the shoals in the river are marked with red circles). The [SPM] are lower within the main waterway than on section line L3 indicated with crosses. The boundary of the waterway can be identified from the curve of the sampled [SPM] on section line L3. Figure 7d shows the distribution of [SPM] near the deep-water waterway in the North Channel, which clearly demonstrates the effects of the training jetty constructed to induce siltation on the spatial distribution of the [SPM].

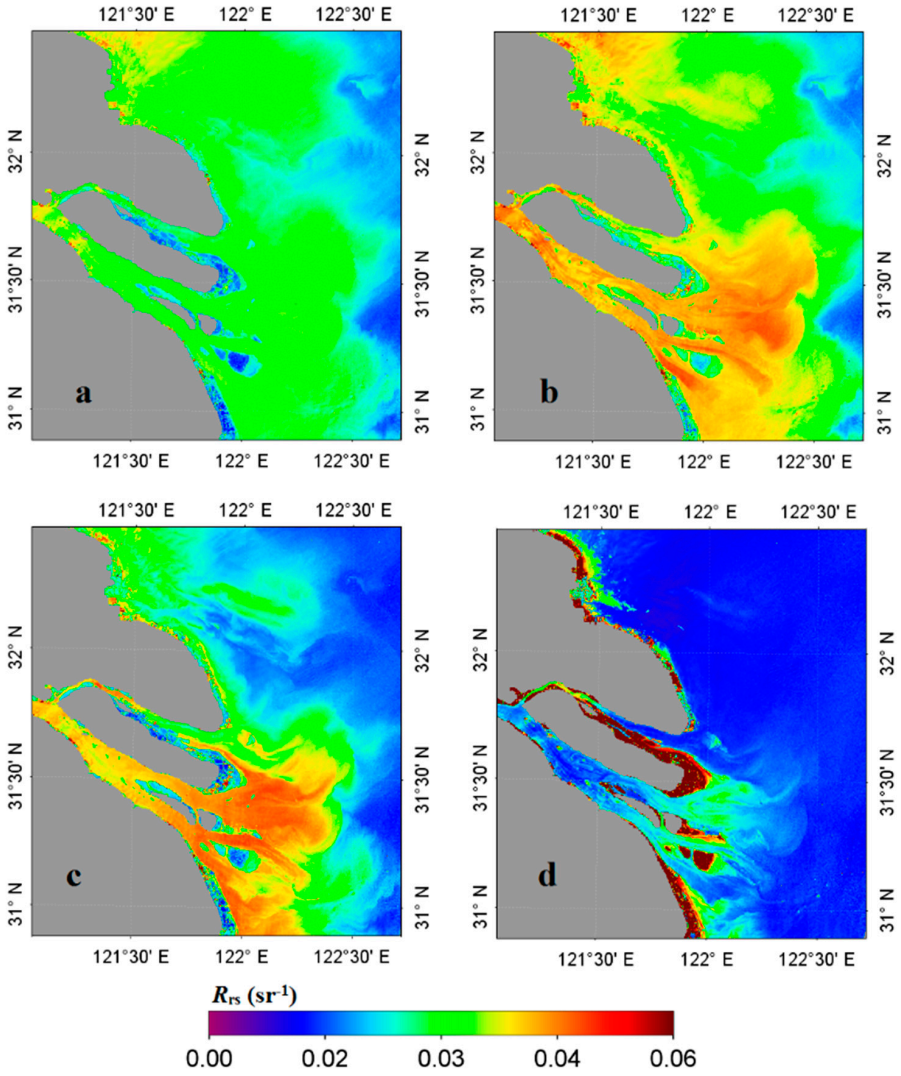

Figure 6. R_{rs} (λ) retrieved from the L8/OLI image at 10:30, 29 August 2013, using the ESOA atmospheric correction method: (**a**) 481 nm; (**b**) 560 nm; (**c**) 655 nm; (**d**) 865 nm. The land masks with 1500-m resolution in SeaDAS were used.

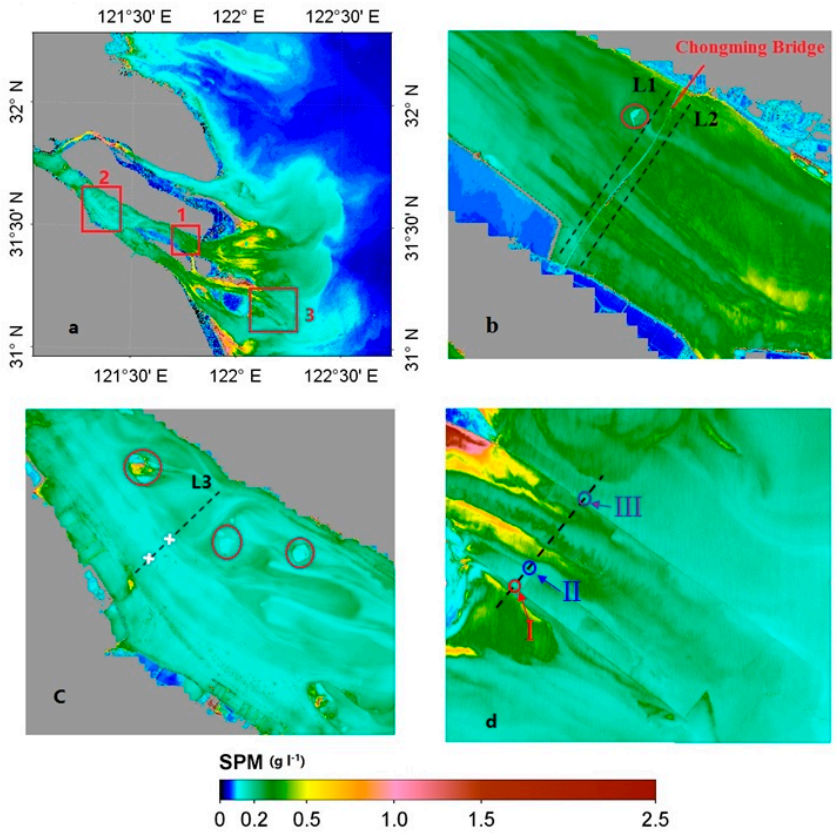

Figure 7. [SPM] retrieved from the L8/OLI L1B images (29 August 2013, 10:30) over the Yangtze estuary (**a**). The numbered boxes show areas selected to show details. Boxes 1, 2 and 3 correspond to (**b**–**d**), respectively. Red circles indicate shoals in the river channel. Dashed black lines are transects, and white crosses indicate the boundaries of the main waterway. The three circles labeled by I, II and III refer to the dam jetties.The land masks with 1500-m resolution in SeaDAS were used.

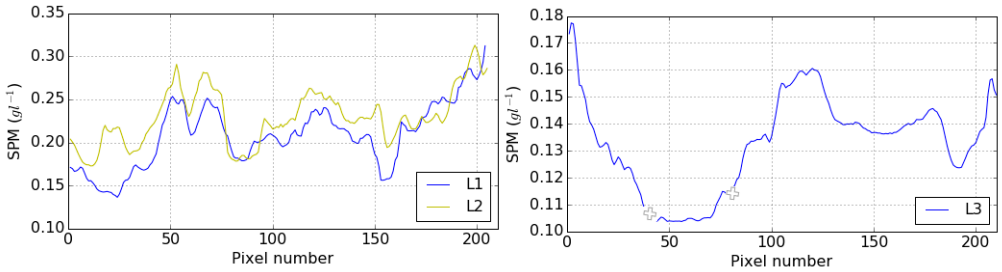

Figure 8. [SPM] along transects L1 and L2 (**left**) and L3 (**right**) in Figure 7b,c, respectively. The white crosses (**right**) correspond to the crosses in Figure 7c.

4.2. Results of Fusion and Prediction

[SPM] images at the L8/OLI resolution were predicted using the method described in Section 3.3. Here, the predicted $[SPM]^{OLI}$ images for four scenes based on the data from August 29 between 09:30 and 12:30 h are qualitatively analyzed. Figure 9 shows the $[SPM]^{OLI}$ images of four scenes in the study area. For ease of comparison, the $[SPM]^{GOCI}$ images at the times corresponding to the $[SPM]^{OLI}$ images are shown on the left. Figure 9a,f (first row) show the observation data-derived $[SPM]^{GOCI}$ and $[SPM]^{OLI}$. Similar spatial distribution patterns are shown in Figure 9 for the predicted $[SPM]^{OLI}$ and derived $[SPM]^{GOCI}$ values at the corresponding times. However, the $[SPM]^{OLI}$ values are generally

slightly higher than the [SPM]^{GOCI} values. The high values in some areas in the images at 11:30 and 12:30 h are caused by clouds.

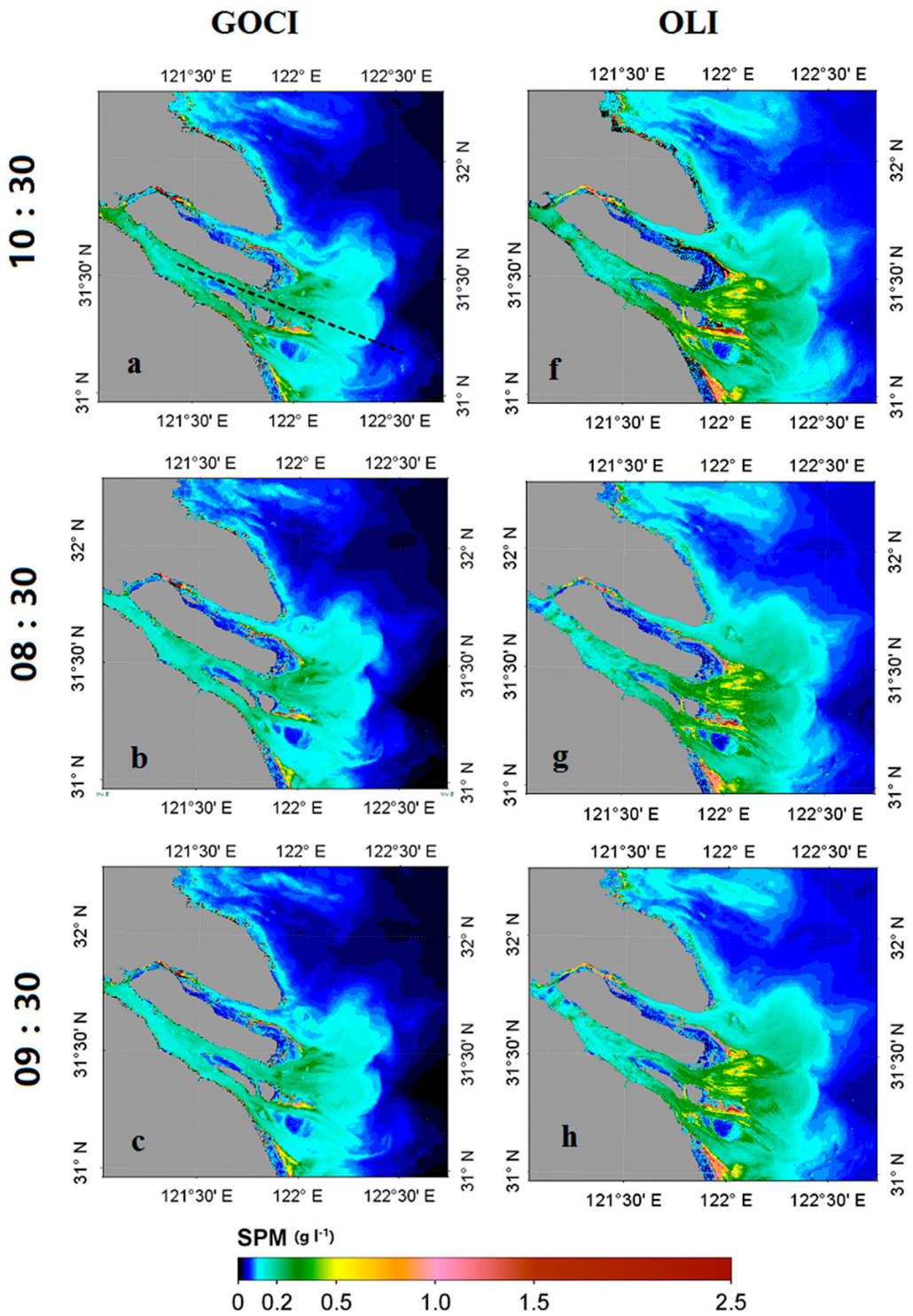

Figure 9. *Cont.*

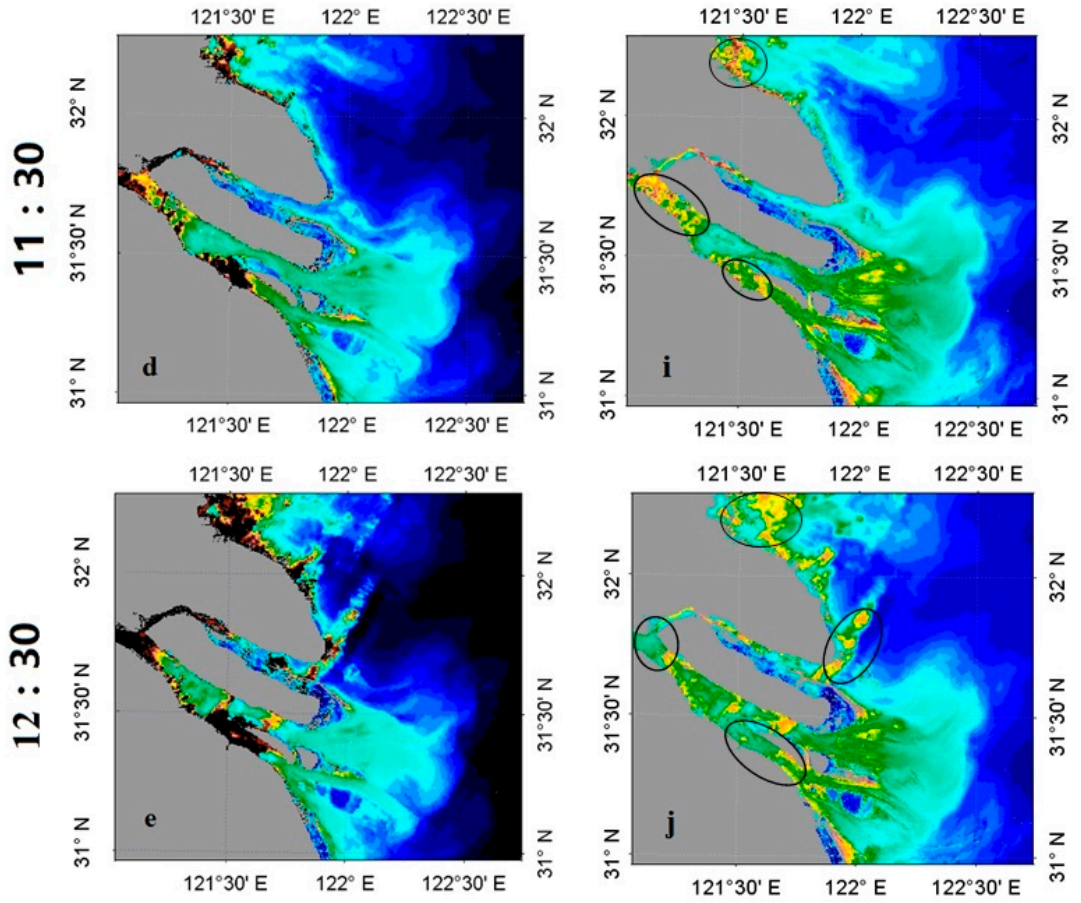

Figure 9. Predicted hourly SPM values at the L8/OLI resolution (**g**–**j**) based on one SPM image pair at 10:30 h (**a**,**f**) and hourly SPM values retrieved from the GOCI images (08:30 (**b**), 09:30 (**c**), 11:30 (**d**) and 12:30 h (**e**)) on 29 August 2013 using the Spatial and Temporal Adaptive Reflectance Fusion Model (STARFM) method. No images were predicted for 13:30, 14:30 and 15:30 h because they contained heavy clouds. The dashed black line in (**a**) is the transect line. The land masks with 1500-m resolution in SeaDAS were used. Black red or black in (**d**,**e**), and the black circled areas in (**i**,**j**) are clouds.

The image near the Chongming Bridge in Figure 7c is enlarged to examine the variations in the spatial and temporal distributions of the predicted $[SPM]^{OLI}$ values (Figure 10). Excellent details of the spatial distribution of the predicted $[SPM]^{OLI}$ values can be observed. We also added a section line through the South Branch, North Channel and largest turbid zone to outside the estuary and subsequently sampled and compared the [SPM] values on this line in the images of 10 scenes in Figure 9 (Figure 11). The solid lines in Figure 11 signify $[SPM]^{GOCI}$, and the dashed lines signify $[SPM]^{OLI}$ (including the predicted values); in addition, different colors signify different times. The solid and dashed lines in Figure 11 show similar trends in which [SPM] decreases, then increases, and then decreases again from within the estuary to the largest turbid zone to outside the estuary. However, the solid lines fluctuate much more than the dashed lines. This suggests that the 30-m spatial resolution $[SPM]^{OLI}$ images display more spatial details than the 500-m spatial resolution $[SPM]^{GOCI}$ images. In addition, the comparison of different times shows similar variation trends between $[SPM]^{OLI}$ and $[SPM]^{GOCI}$. This indicates that the predicted $[SPM]^{OLI}$ images not only maintain the advantage of high spatial resolution but also have a high temporal resolution.

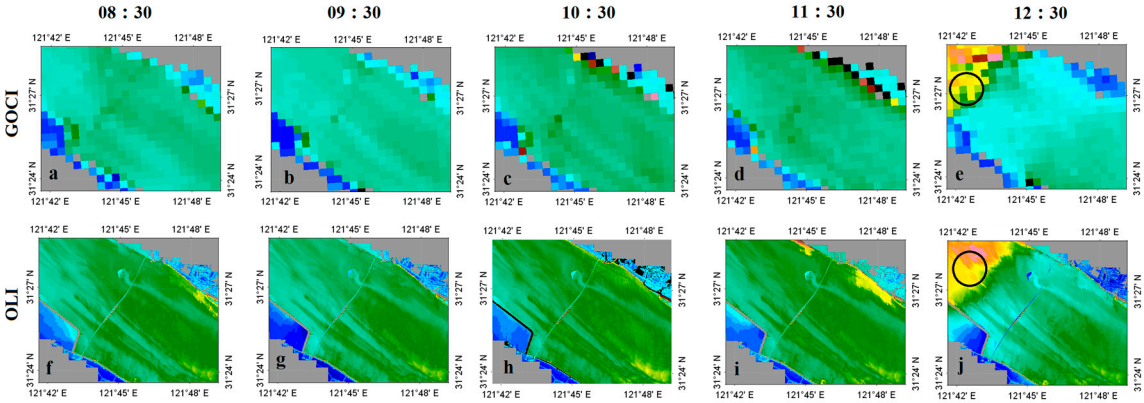

Figure 10. Detailed spatial distributions of $[SPM]^{GOCI}$ (**a**–**e**) retrieved from the GOCI L1B images on 29 August 2013, and retrieved (**h**) and predicted $[SPM]^{OLI}$ (**f**,**g**,**i**,**j**) over the area of box 1 in Figure 7b. The $[SPM]^{OLI}$ values at 10:30 were retrieved from the L8/OLI L1B image, and the others are predicted images. The black circled area in (**e**) is a cloudy area.

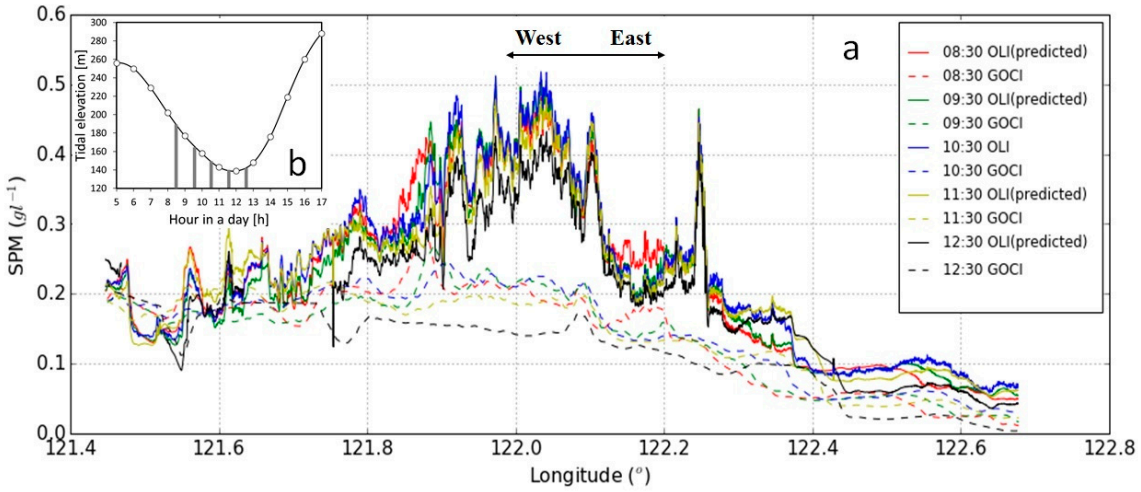

Figure 11. Comparison of $[SPM]^{OLI}$ (solid) and $[SPM]^{GOCI}$ (dashed) values along the section (dashed black line) in Figure 9a. Different colors refer to different times of sensors imaging. For the SPM at 12:30 h, some cloudy pixels are not shown. The sub-plot at the upper left corner shows the hourly tidal elevation data from the "Zhongjun" tide gauge station in the same day of the GOCI data.

To quantitatively evaluate their accuracy, the predicted $[SPM]^{OLI}$ values are cross-compared with the [SPM] measured by OBSs at the fixed field stations and the $[SPM]^{GOCI}$ values (Figure 12). It should be noted that the [SPM] data collected at the Baozhen station on 13 August and 17 November are not used due to recording anomalies; thus, 32 image-matched measurement pairs were available. Compared to the [SPM] collected at the OBSs, the MRE values for $[SPM]^{OLI}$ and $[SPM]^{GOCI}$ are 17.7% and 27.5% (Figure 12a), respectively. Figure 12b shows scatter plots of the $[SPM]^{OLI}$ and $[SPM]^{GOCI}$ values. Figure 13 shows the time series of the predicted $[SPM]^{OLI}$ values based on different images and measurements taken at different OBSs and the [SPM] measured by the OBSs. The predicted and measured [SPM] values have generally consistent variation trends and similar values (Figure 13). The errors in the predicted [SPM] at the Changxingdao station at 15:30 on 13 August and 17 November are relatively large due to clouds.

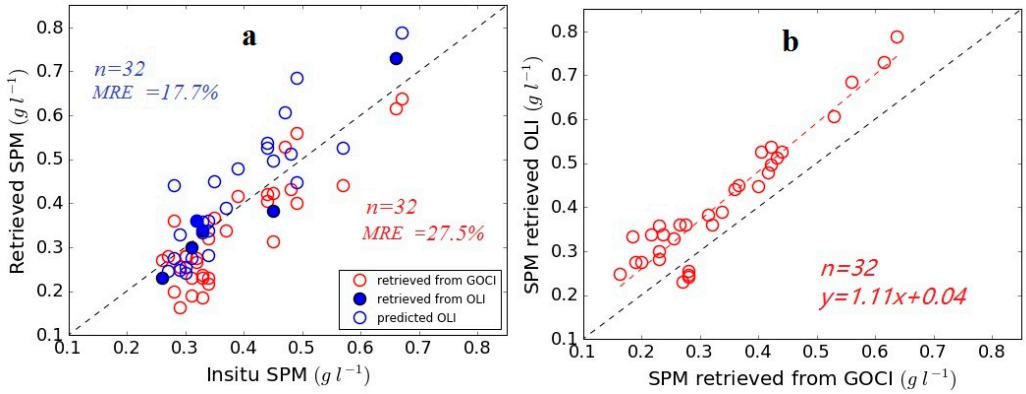

Figure 12. (**a**) Comparison of SPM retrieved from satellite images with SPM observed by observation stations (OBSs) at fixed stations. Red circles refer to SPM retrieved from GOCI, and blue circles and filled blue circles refer to SPM retrieved from L8/OLI and predicted SPM, respectively; (**b**) Comparison of SPM retrieved from GOCI and L8/OLI at fixed stations.

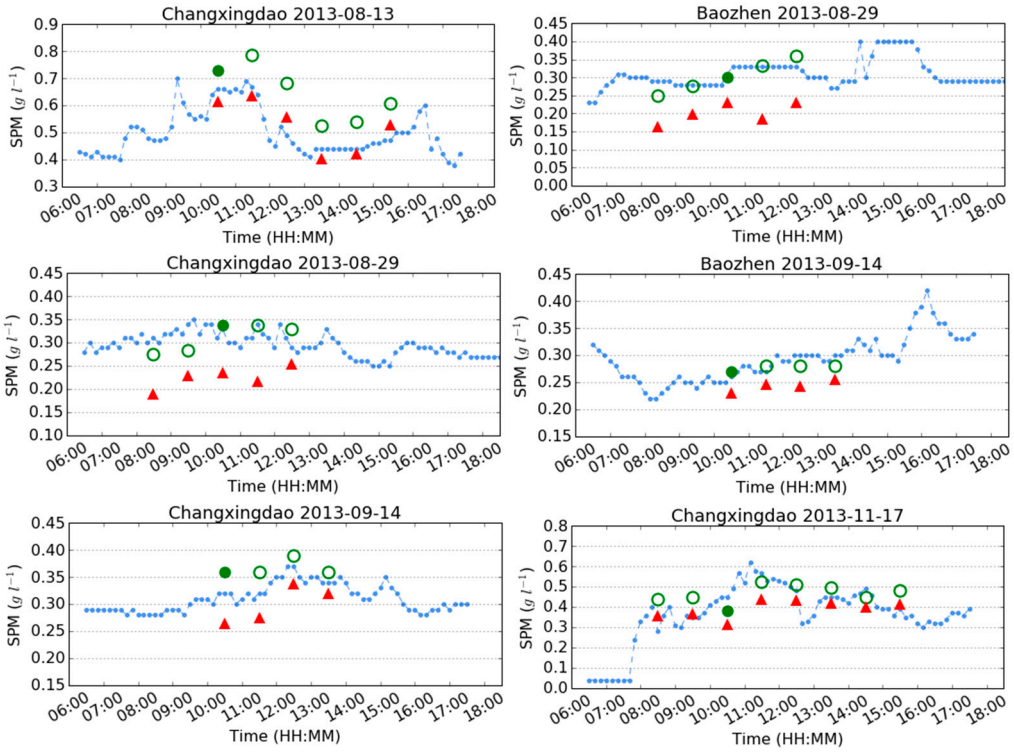

Figure 13. Comparison of the SPM retrieved from GOCI hourly images and the predicted SPM at the L8/OLI resolution based on STARFM at each fixed station. The *X*-axis and *Y*-axis refer to time and [SPM], respectively. The blue dotted line represents the OBS-measured SPM over time, the red triangles represent $[SPM]^{GOCI}$ values, the filled green circles represent the retrieved $[SPM]^{OLI}$ values, and the open green circles represent the predicted $[SPM]^{OLI}$.

5. Discussion

5.1. Error Sources and Limitations

If the TOA radiances of the two sensors (L8/OLI and GOCI) are assumed to be well calibrated, the errors of the predicted and derived SPM mainly come from the following three sources: the

atmospheric correction, the retrieval algorithm of the SPM, and the temporal and spatial fusion algorithm STARFM.

The SPM is retrieved by the semi-experimental model SERT, which neglects the variations of the chlorophyll-a concentration ([Chl-a]) and colored dissolved organic matter (CDOM); this may cause errors in the derived SPM. According to Pan et al. [35], the errors decrease as the [SPM] increases. When the [SPM] reaches 0.5 g L^{-1}, the errors in the derived SPM caused by the variations of Chl-a and CDOM will not exceed 10%. In this study, the three bands used to retrieve the SPM are very close; the maximum difference between the wavelengths is not more than 6 nm, which suggests that the difference between the retrieved $[SPM]^{GOCI}$ and $[SPM]^{OLI}$ values mainly comes from the atmospheric correction.

In this study, the aerosol type and AOD are estimated by ESOA. The coupled model in ESOA is based on the AERONET-based aerosol model and the SERT model. Although the AERONET-based aerosol model contains several aerosol types, including heavily absorbing aerosols, no AERONET stations are located in the Yangtze estuary; therefore, whether the aerosol types in the study area are included in the AERONET-based aerosol model is still unknown. Furthermore, the SERT model assumes that the R_{rs} spectrum is completely determined by the [SPM]; CDOM and chlorophyll are assumed to be constant. Although the errors in R_{rs} ($\lambda > 550$ nm) caused by the variations of CDOM and [Chl-a] are not more than 30% [35], the errors exist. The aerosol type and AOT derived from ESOA may produce some errors. However, because the GOCI images (10:30) and L8/OLI (10:30) images use the same aerosol parameters for the atmospheric correction, the errors in the derived aerosol parameters will not produce large differences between the GOCI- and L8/OLI-derived R_{rs} values. In addition to aerosol estimation, the other terms involved in the atmospheric correction procedure implemented in l2gen may also produce errors. For example, the calculation of the BRDF correction factor in the current version of l2gen is still based on Case 1 waters, and the NIR water-leaving radiance is assumed to be 0 [37]. Therefore, the value of the BRDF correction factor is 0 at wavelengths of 745 nm and 865 nm in the GOCI images and at the wavelength of 865 nm in the L8/OLI images. This algorithm will generate errors when it is used in the Yangtze estuary. All of these errors may produce errors in the derived R_{rs} values and contribute to the differences between the R_{rs} values retrieved from L8/OLI and GOCI in the study area. However, the main reason is still unknown, and how to eliminate the difference remains a problem.

The STARFM model is used to blend the $[SPM]^{GOCI}$ and $[SPM]^{OLI}$ images, which have spatial resolutions of 500 m and 30 m, respectively. As we discussed previously, it is reasonable to use the STARFM model for waters, even highly dynamic waters. This study has provided several positive results. However, the STARFM model has several potential limitations. If the changes are too subtle to be detected by the GOCI observations, this algorithm will not be able to predict any changes when synthesizing the fine resolution imagery. Furthermore, there may be situations in which the STARFM algorithm cannot detect changes, such as when two contradicting changes occur simultaneously within a coarse-resolution pixel and compensate for each other. In addition, only one pair of L8/OLI- and GOCI-derived SPM images is used as the base imagery pair in this study. Although it is capable of capturing the changes in the SPM distribution patterns to some extent, the prediction will be improved if more than one image pair is used. Furthermore, the STARFM algorithm neglects geolocation errors, which always exist. For example, the registration of two images observed by different sensors will produce geolocations errors. These errors will affect the predictions.

5.2. The Spatiotemporal Variations of [SPM]

As was shown in Figure 9 that the spatial heterogeneity of the predicted $[SPM]^{OLI}$ distribution was relatively higher than that of $[SPM]^{GOCI}$, especially in the maximum turbidity zone of the Yangtze Estuary. It was found in Figure 11 that the spatial variation of [SPM] in the east of 122.4°N was relatively weak, which was in accordance with the observed results of $[SPM]^{GOCI}$. This phenomenon was dominated by the marine water mass in the offshore of the Yangtze Estuary and less sediment

discharge from the Yangtze River [47]. At the same time, the predicted $[SPM]^{OLI}$ in the west of 121.7°N was basically consistent with $[SPM]^{GOCI}$, which was slightly higher than that in the east of 122.4°N since it is mainly controlled by the river runoff and sediment discharge in the upper reaches of the Yangtze River [44,48]. The section from 121.7°N to 122.4°N is located in the maximum turbidity zone of the Yangtze Estuary, with the highest [SPM] and relatively large spatiotemporal variations. It results from the intense interaction between the river runoff and tidal currents in the maximum turbidity zone of the Yangtze Estuary that leads to resuspension of bottom sediments [49]. The exchange of materials and waters between the channels and tidal flats was strong under complex hydrodynamic conditions [48,50]. This implies a need for the observation with both of the high spatial and temporal resolution data. Obviously, the predicted $[SPM]^{OLI}$ can reflect the dramatic temporal and spatial changes in the natural state of the Yangtze Estuary. However, GOCI observation at the spatial resolution of 500 m cannot depict the details of [SPM] spatial distribution.

Furthermore, the predicted $[SPM]^{OLI}$ image can also show the profound impact of the construction of the Deep Waterway Project (DWP) on the [SPM] spatial and temporal distribution. To illustrate this point, we added a section line to the DWP in the North Passage in Figure 7d (see black dotted line). It was shown in Figure 7d that the [SPM] presented a remarkable strip along the DWP dams' direction. The obvious edges of its transition were the locations of the DWP jetties [51,52], which were also located in the spikes labeled by I, II and III in Figure 7d. From the view of the cross-section shown in Figure 14 that the [SPM] was very high with argely spatial variations in the DWP between II and III jetties. The dams and leading jetties intercepted SPM and meanwhile changed current regimes of the waterway, so that the [SPM] exhibited a high heterogeneity of spatiotemporal distribution. In addition, the turbulence around the piers resulted in the decrease trend of [SPM] in the piers (Figure 10). Clearly, GOCI with coarse spatial resolution cannot observe the subtle inhomogeneous distribution.

Both of Figures 11 and 14 showed that the [SPM] increased from 08:30 h (red line and dash-line), reached the maximum at 10:30 (blue line and dash-line), and then decreased from 10:30 to 12:30 (black line and dash-line). These variations were linked to the change of the daily tidal elevation (see the subplot in the left upper corner of Figure 11). More interestingly, comparing with the fusion prediction of high-resolution [SPM], GOCI-derived [SPM] have the same hourly variation pattern. However, when it comes to the details of [SPM] spatial distribution, GOCI lost details, especially for impacts of human engineering on [SPM] spatial distribution. The [SPM] increased with the decrease of the tidal level, but the change trend of the [SPM] was slightly delayed corresponding to the change rate of tidal level. This situation was consistent with the previously reports [15,44].

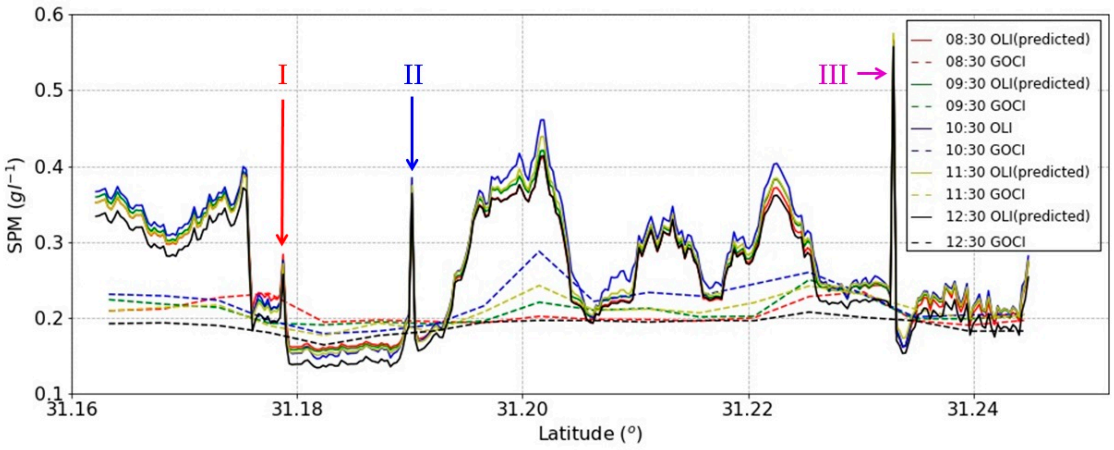

Figure 14. Same as Figure 11, but for the section (dashed black line) in Figure 7d. I, II and III correspond to the dam jetties in Figure 7d.

6. Conclusions

The Yangtze estuarine and coastal waters are marked by a complex hydrodynamic environment and frequent variations in the spatial and temporal distributions of the [SPM]. The study of the dynamic variations in the spatial and temporal distributions of the [SPM] in the Yangtze estuary using a single satellite sensor, such as a geostationary orbit sensor (e.g., the GOCI) or a high-spatial-resolution sensor (e.g., the L8/OLI), will be limited by deficiencies in the observation frequency and spatial resolution of the satellite. In this study, [SPM] images with both the high temporal resolution provided by the GOCI and the high spatial resolution provided by the L8/OLI were generated using the classical STARFM model from a product-level fusion perspective. The results show that the predicted [SPM] images are capable of showing the spatial details of [SPM] in the estuary with hourly temporal variations. In addition, the [SPM] predicted from the fused images exhibit higher accuracy.

More importantly, thanks to the derived high-resolution [SPM] images with high spatiotemporal dynamic changes, both natural phenomena (dynamic variation of the maximum turbid zone) and human engineering changes leading to the dynamic variability of SPM in the channel, are observed. This provides a new opportunity to study the spatial and temporal variations in [SPM] in estuaries, particularly at the channel level, without the need to increase the spatial and temporal resolutions of the sensors. However, imperfect atmospheric corrections greatly increase the uncertainty of the predicted [SPM]. Therefore, further research is required to address the inconsistency in the atmospheric corrections of various sensors, particularly polar and geostationary orbit satellite sensors.

Acknowledgments: This study is supported by National Key R&D Program of China (no. 2016YFE0103200) and NSFC projects (no. 41771378, 51739005). The research is part of the HYPERMAQ project (SR/00/335) of the BELSPO Research programme for earth Observation STEREO III, commissioned and financed by the Belgian Science Policy Office. The USGS and NASA are thanked for the Landsat-8 imagery. NASA is thanked for the SeaDAS processing software and its source code, and KORDI/KOSC is thanked for the GOCI imagery. USDA-ARS is thanked for the STARFM source code. The Remote Sensing and Ecosystem Modelling (REMSEM) team of the Royal Belgian Institute of Natural Sciences is thanked for the ACOLITE software. The authors also thank four anonymous reviewers for their helpful comments and suggestions.

Author Contributions: Yanqun Pan and Fang Shen conceived and designed the study. Fang Shen provided part of the in situ data. Yanqun Pan wrote the programs and performed the experiments, the results were examined by Fang Shen. All authors contributed to the writing and approved the final manuscript.

Conflicts of Interest: The authors declare no conflict of interest.

References

1. Van Der Wal, D.; Pye, K.; Neal, A. Long-term morphological change in the Ribble Estuary, northwest England. *Mar. Geol.* **2002**, *189*, 249–266. [CrossRef]
2. Li, S.; Yun, C. A Study on the Quantitative Model of the Suspended Sediment Concentration from the Meteorological Satellite Imagery. *J. Remote Sens.* **2001**, *5*, 154. [CrossRef]
3. Liu, X.; Shen, F.; Zhu, W.; Liu, X. Quantitative Retrieval for Suspended Sediment Concentration by using MERIS Satellite Data in the YANGTZE River Estuary. *Resour. Environ. Yangtze Basin* **2009**, *18*, 1026–1030.
4. Bulletin of China River Sediment (BCRS), 2010–2011: Press of Ministry of Water Resources of the People's Republic of China. Available online: http://www.cjh.com.cn (accessed on 10 June 2016).
5. Guo, X. *Characteristics of Recent Tidal Current and Suspended Sediment Concentration Distribution and Sediment Transport in the Yangtze Estuary*; East China Normal University: Shanghai, China, 2013.
6. Sinica, A.G.; Estuary, T. Trends and causes of suspended sediment concentration variation in the turbidity maximum zone at the Yangtze River Estuary. *Acta Geogr. Sin.* **2013**, *68*, 1240–1250. [CrossRef]
7. Jiang, C.; Li, J.; Swart, H.E.D. Effects of navigational works on morphological changes in the bar area of the Yangtze Estuary. *Geomorphology* **2016**, *139–140*, 205–219. [CrossRef]
8. Tan, Z.W.; Fan, Q.J. Analysis of reasons for the siltation in North Passage of Yangtze Estuary. *Port Waterw. Eng.* **2011**, *1*, 29–34.

9. Liu, G.; Zhu, J.; Wang, Y.; Wu, H.; Wu, J. Tripod measured residual currents and sediment flux: Impacts on the silting of the Deepwater Navigation Channel in the Changjiang Estuary. *Estuar. Coast. Shelf Sci.* **2011**, *93*, 192–201. [CrossRef]
10. Cai, L.; Tang, D.; Levy, G.; Liu, D. Remote sensing of the impacts of construction in coastal waters on suspended particulate matter concentration—The case of the Yangtze River delta, China. *Int. J. Remote Sens.* **2015**, *1161*, 1–16. [CrossRef]
11. Manzo, C. Sensitivity analysis of a bio-optical model for Italian lakes focused on Landsat-8, Sentinel-2 and Sentinel-3. *Eur. J. Remote Sens.* **2015**, *48*, 17–32. [CrossRef]
12. Concha, J.A.; Schott, J.R. Retrieval of color producing agents in Case 2 waters using Landsat 8. *Remote Sens. Environ.* **2016**, *185*, 95–107. [CrossRef]
13. Vanhellemont, Q.; Ruddick, K. Turbid wakes associated with offshore wind turbines observed with Landsat 8. *Remote Sens. Environ.* **2014**, *145*, 105–115. [CrossRef]
14. He, X.; Bai, Y.; Pan, D.; Huang, N.; Dong, X.; Chen, J.; Chen, C.T.; Cui, Q. Using geostationary satellite ocean color data to map the diurnal dynamics of suspended particulate matter in coastal waters. *Remote Sens. Environ.* **2013**, *133*, 225–239. [CrossRef]
15. Hu, Z.; Pan, D.; He, X.; Bai, Y. Diurnal Variability of Turbidity Fronts Observed by Geostationary Satellite Ocean Color Remote Sensing. *Remote Sens.* **2016**, *8*, 147. [CrossRef]
16. Guo, L.; Wegen, M.; van der Jay, D.A.; Matte, P.; Wang, Z.B.; Roelvink, D.; He, Q. River-tide dynamics: Exploration of nonstationary and nonlinear tidal behavior in the Yangtze River estuary Leicheng. *J. Geophys. Res. Oceans* **2015**, *120*, 3499–3521. [CrossRef]
17. Gao, F.; Masek, J.; Schwaller, M.; Hall, F. On the blending of the landsat and MODIS surface reflectance: Predicting daily landsat surface reflectance. *IEEE Trans. Geosci. Remote Sens.* **2006**, *44*, 2207–2218. [CrossRef]
18. Zhu, X.; Chen, J.; Gao, F.; Chen, X.; Masek, J.G. An enhanced spatial and temporal adaptive reflectance fusion model for complex heterogeneous regions. *Remote Sens. Environ.* **2010**, *114*, 2610–2623. [CrossRef]
19. Hilker, T.; Wulder, M.A.; Coops, N.C.; Linke, J.; McDermid, G.; Masek, J.G.; Gao, F.; White, J.C. A new data fusion model for high spatial- and temporal-resolution mapping of forest disturbance based on Landsat and MODIS. *Remote Sens. Environ.* **2009**, *113*, 1613–1627. [CrossRef]
20. Huang, B.; Song, H. Spatiotemporal reflectance fusion via sparse representation 2012. *IEEE Trans. Geosci. Remote Sens.* **2012**, *50*, 3707–3716. [CrossRef]
21. Zhang, H.K.; Huang, B.; Zhang, M.; Cao, K.; Yu, L. A generalization of spatial and temporal fusion methods for remotely sensed surface parameters. *Int. J. Remote Sens.* **2015**, *36*, 4411–4445. [CrossRef]
22. Vanhellemont, Q.; Neukermans, G.; Ruddick, K. Synergy between polar-orbiting and geostationary sensors: Remote sensing of the ocean at high spatial and high temporal resolution. *Remote Sens. Environ.* **2013**, *146*, 49–62. [CrossRef]
23. Wang, Z. *Recent Temporal and Spatial Variations and Transport Processes of Suspended Sediment in the North Passage of the Yangtze River Estuary*; East China Normal University: Shanghai, China, 2013.
24. Jie, Z.; He, Q.; Wang, X.; Guo, L.-C. Field Observations on the Characteristics of Current and Sediment of the South and North Branches in the Yangtze Estuary. *Resour. Environ. Yangtze Basin* **2015**, *24*, 21–27.
25. Choi, J.; Park, Y.J.; Ahn, J.H.; Lim, H.; Eom, J.; Ryu, J. GOCI, the world's first geostationary ocean color observation satellite, for the monitoring of temporal variability in coastal water turbidity. *J. Geophys. Res. Oceans* **2012**, *117*, 1–10. [CrossRef]
26. Franz, B.A.; Bailey, S.W.; Kuring, N.; Werdell, P.J. Ocean color measurements with the Operational Land Imager on Landsat-8: Implementation and evaluation in SeaDAS. *J. Appl. Remote Sens.* **2015**, *9*. [CrossRef]
27. Pahlevan, N.; Lee, Z.; Wei, J.; Schaaf, C.B.; Schott, J.R.; Berk, A. On-orbit radiometric characterization of OLI (Landsat-8) for applications in aquatic remote sensing. *Remote Sens. Environ.* **2014**, *154*, 272–284. [CrossRef]
28. Zhang, Y.; Zhang, Y.; Shi, K.; Zha, Y.; Zhou, Y.; Liu, M. A Landsat 8 OLI-Based, Semianalytical Model for Estimating the Total Suspended Matter Concentration in the Slightly Turbid Xin'anjiang Reservoir (China). *IEEE J. Sel. Top. Appl. Earth Obs. Remote Sens.* **2016**, *9*, 398–413. [CrossRef]
29. Zhang, C.; Han, M.I.N. Mapping Chlorophyll-a Concentration in Laizhou Bay Using Landsat 8 OLI data. In Proceedings of the 36th IAHR World Congress, the Hague, The Netherlands, 28 June–3 July 2015; pp. 1–6.
30. Olmanson, L.G.; Brezonik, P.L.; Finlay, J.C.; Bauer, M.E. Comparison of Landsat 8 and Landsat 7 for regional measurements of CDOM and water clarity in lakes. *Remote Sens. Environ.* **2016**, *185*, 119–128. [CrossRef]

31. Ody, A.; Doxaran, D.; Vanhellemont, Q.; Nechad, B.; Novoa, S.; Many, G.; Bourrin, F.; Verney, R.; Pairaud, I.; Gentili, B. Potential of high spatial and temporal ocean color satellite data to study the dynamics of suspended particles in a micro-tidal river plume 2016. *Remote Sens.* **2016**, *8*, 245. [CrossRef]
32. Han, B.; Loisel, H.; Vantrepotte, V.; Mériaux, X.; Bryère, P.; Ouillon, S.; Dessailly, D.; Xing, Q.; Zhu, J. Development of a Semi-Analytical Algorithm for the Retrieval of Suspended Particulate Matter from Remote Sensing over Clear to Very Turbid Waters. *Remote Sens.* **2016**, *8*, 211. [CrossRef]
33. Vanhellemont, Q.; Ruddick, K. Advantages of high quality SWIR bands for ocean colour processing: Examples from Landsat-8. *Remote Sens. Environ.* **2015**, *161*, 89–106. [CrossRef]
34. Xue, Y.Z.; Qing, H.E.; Wang, Y.Y. The method and application of OBS in the measureme nt of sediment Concentration. *J. Sediment Res.* **2004**, *4*, 56–60.
35. Pan, Y.; Shen, F.; Verhoef, W. An improved spectral optimization algorithm for atmospheric correction over turbid coastal waters: A case study from the Changjiang (Yangtze) estuary and the adjacent coast. *Remote Sens. Environ.* **2017**, *191*, 197–214. [CrossRef]
36. Shen, F.; Verhoef, W.; Zhou, Y.; Salama, M.S.; Liu, X. (SERT)Satellite Estimates of Wide-Range Suspended Sediment Concentrations in Changjiang (Yangtze) Estuary Using MERIS Data. *Estuar. Coasts* **2010**, *33*, 1420–1429. [CrossRef]
37. Mobley, C.D.; Werdell, J.; Franz, B.; Ahmad, Z.; Bailey, S. *Atmospheric Correction for Satellite Ocean Color Radiometry*. A Tutorial and Documentation; 2016; pp. 1–73. Available online: http://www.oceanopticsbook.info/view/atmospheric_correction/chapter_overview (accessed on 10 September 2016).
38. Vanhellemont, Q.; Bailey, S.; Franz, B.; Shea, D. Atmospheric Correction of Landsat-8 Imagery Using Seadas. In Proceedings of the Sentinel-2 for Science Workshop, Frascati, Italy, 20–23 May 2014.
39. Shen, F.; Zhou, Y.; Peng, X.; Chen, Y. Satellite multi-sensor mapping of suspended particulate matter in turbid estuarine and coastal ocean, China. *Int. J. Remote Sens.* **2014**, *35*, 4173–4192. [CrossRef]
40. Hooker, S.B.; Lazin, G.; Zibordi, G.; Mclean, S. An evaluation of above- and in-water methods for determining water-leaving radiances. *J. Atmos. Ocean. Technol.* **2002**, *19*, 486–515. [CrossRef]
41. Mobley, C.D. Estimation of the remote-sensing reflectance from above-surface measurements. *Appl. Opt.* **1999**, *38*, 7442–7455. [CrossRef] [PubMed]
42. Sokoletsky, L.G.; Shen, F. Optical closure for remote-sensing reflectance based on accurate radiative transfer approximations: The case of the Changjiang (Yangtze) River Estuary and its adjacent coastal area, China. *Int. J. Remote Sens.* **2014**, *35*, 4193–4224. [CrossRef]
43. Shang, P.; Shen, F. Atmospheric Correction of Satellite GF-1/WFV Imagery and Quantitative Estimation of Suspended Particulate Matter in the Yangtze Estuary. *Sensors* **2016**, *16*, 1997. [CrossRef] [PubMed]
44. Shen, F.; Zhou, Y.X.; Li, J.F.; He, Q.; Verhoef, W. Remotely sensed variability of the suspended sediment concentration and its response to decreased river discharge in the Yangtze estuary and adjacent coast. *Cont. Shelf Res.* **2013**, *69*, 52–61. [CrossRef]
45. Gevaert, C.M.; García-Haro, F.J. A comparison of STARFM and an unmixing-based algorithm for Landsat and MODIS data fusion. *Remote Sens. Environ.* **2015**, *156*, 34–44. [CrossRef]
46. Weng, Q.; Fu, P.; Gao, F. Generating daily land surface temperature at Landsat resolution by fusing Landsat and MODIS data. *Remote Sens. Environ.* **2014**, *145*, 55–67. [CrossRef]
47. Liu, J.P.; Xu, K.H.; Li, A.C.; Milliman, J.D.; Velozzi, D.M.; Xiao, S.B.; Yang, Z.S. Flux and fate of Yangtze River sediment delivered to the East China Sea. *Geomorphology* **2007**, *85*, 208–224. [CrossRef]
48. Dai, Z.; Fagherazzi, S.; Mei, X.; Gao, J. Decline in suspended sediment concentration delivered by the Changjiang (Yangtze) River into the East China Sea between 1956 and 2013. *Geomorphology* **2016**, *268*, 123–132. [CrossRef]
49. Ge, J.; Shen, F.; Guo, W.; Chen, C.; Ding, P. Estimation of critical shear stress for erosion in the Changjiang Estuary: A synergy research of observation, GOCI sensing and modeling. *J. Geophys. Res. Oceans* **2015**, *120*, 8439–8465. [CrossRef]
50. Chen, S.L.; Zhang, G.A.; Yang, S.L.; Shi, J.Z. Temporal variations of fine suspended sediment concentration in the Changjiang River estuary and adjacent coastal waters, China. *J. Hydrol.* **2006**, *331*, 137–145. [CrossRef]

51. Luan, H.L.; Ding, P.X.; Wang, Z.B.; Ge, J.Z.; Yang, S.L. Decadal morphological evolution of the Yangtze Estuary in response to river input changes and estuarine engineering projects. *Geomorphology* **2016**, *265*, 12–23. [CrossRef]
52. Ge, J.; Chen, C.; Qi, J.; Ding, P.; Beardsley, R.C. A dike-groyne algorithm in a terrain-following coordinate ocean model (FVCOM): Development, validation and application. *Ocean Model.* **2012**, *47*, 26–40. [CrossRef]